



Cu dendrites induced by the Anderson-type polyoxometalate $\text{NiMo}_6\text{O}_{24}$ as a promising electrocatalyst for enhanced hydrogen evolution



Dejin Zang^a, Yichao Huang^a, Qi Li^a, Yajie Tang^b, Yongge Wei^{a,*}

^a Key Lab of Organic Optoelectronics & Molecular Engineering of Ministry of Education, Department of Chemistry, Tsinghua University, Beijing 100084, PR China

^b Key Laboratory of Fermentation Engineering (Ministry of Education), Hubei Provincial Cooperative Innovation Center of Industrial Fermentation, Hubei Key Laboratory of Industrial Microbiology, Hubei University of Technology, Wuhan 430068, PR China

ARTICLE INFO

Keywords:

Cu dendrites
Polyoxometalates
Decreased overpotential
HER

ABSTRACT

The design and synthesis of specific functional complex materials as desired catalysts for improved energy conversion and storage are of great importance and with grand challenges. Here, a facile synthesis strategy of Anderson POMs supported Cu dendrites toward electrochemical hydrogen evolution reaction with dramatically decreased overpotential under acidic aqueous condition is established in this work. We present the preparation of well crystallized Cu dendrites through co-electrodeposition on TiO_2 array with Anderson-type POM $\text{NiMo}_6\text{O}_{24}$. Structural and state of valence investigation of the as-obtained electrocatalyst ($\text{NiMo}_6\text{O}_{24}@\text{Cu/TNA}$) evidence the specific morphology tunability and modification of Cu dendrites surfaces. During HER course, $\text{NiMo}_6\text{O}_{24}$ can improve the H^+ transfer and further help the H atom absorption which remedies the weakness of insufficient H atom absorption ability of Cu along with its strong electron transfer lowering overpotential upon HER. Therefore, HER with $\text{NiMo}_6\text{O}_{24}@\text{Cu/TNA}$ is considerably enhanced by decreasing related overpotential of 130 mV compared to porous Cu foam. The modification of $\text{NiMo}_6\text{O}_{24}$ endowed catalysts strong corrosion resistance assuring long term stability. Hence, the proposed strategy possesses improved activity and long term stability upon HER with $\text{NiMo}_6\text{O}_{24}@\text{Cu/TNA}$ as electrocatalyst. Depending on the diversity of POMs, the current feasible and reliable heterogeneous electrocatalysts design with POMs would inspire more effective, low-cost strategies for energy conversion and open the pathway for large scale production.

1. Introduction

Heterogeneous catalytic redox reactions which occur at the electrified interfaces are of extraordinary importance for the performance of many electrochemical devices to future sustainable development strategy and renewable energy conversion/storage [1,2]. Most importantly, the local chemical environment around electrodes and interfaces between electrode and electrolyte essentially determine the activity and efficiency of electrolyzers for energy conversion [3,4]. Wherever, the required electrocatalysts have to be formed with multiple components, in which multiple components are integrated in one catalyst structure to achieve more desirable properties promoting the principal active component's activity [5,6]. The increase in structural complexity poses scientific challenges in understanding the roles of the constituents and their interactions at the interfaces. Making use of multiple components, the electronic and chemical interactions between them within a catalyst structure to unlock unprecedented catalytic functionalities is scientifically intriguing and practically useful but

remains highly challenging [7].

Up to now, hydrogen evolution reaction (HER) still highly depends on the electrocatalysts based on Pt materials, which are scarcity on earth and quite expensive. Thus, more abundant, low-cost, efficient and durable electrocatalysts are in urgent requirement for the supply of clean hydrogen energy [8]. As a promising material, copper is similarly active analogue to platinum but more abundant storage on earth. However, it only has limited activity toward HER due to its deficiency to capture H atoms. Many efforts have been put into preparing copper-transition metal (Cu-M) alloy [9–11] to overcome this issue to improve the HER performance. Accurate identification of the HER active sites on these electrocatalysts and the advances in nanotechnology are jointly contribute to the development of nanostructured electrocatalysts for HER [12]. Moreover, Cu associated with some non-metallic materials (e.g. carbon based materials) which are of unique electronic properties have been also applied as catalysts for electrocatalytic or photocatalytic HER [13–15]. Taking all the above works together, we can predict that with the controllable modulation of the nanostructures and

* Corresponding author.

E-mail address: yonggewei@tsinghua.edu.cn (Y. Wei).

morphologies of Cu-based materials plus the modification of relevant local chemical environment, the HER performance of Cu-based materials should be further improved, which is of great significance to the synthetic chemistry and energy-related applications.

Polyoxometalates (POMs) are a special class of well-defined molecular metal oxide clusters with a wide range of applications in medicine, catalysis, materials sciences, etc [16]. As it is well-known that POMs can function as electron reservoir, this is favorable for multi electrons transfer reaction [17]. They can also act as Brønsted acid which can offer H atoms intrinsically [18]. In the past few years, POMs have been applied to modify electrodes for HER which can give comparable activity to the Pt electrode because of their unique electronic properties [3,19–21]. As a class of polyanions, they are able to induce specific morphology formation meanwhile stabilize the obtained inorganic nanoparticles or organic-inorganic assemblies at the corresponding surfaces [22]. Therefore, in the view of material science, POMs are proper candidates for designing inorganic functional materials for energy conversion.

In this work, we fabricated the Anderson-type POM $(\text{NH}_4)_4[\text{H}_6\text{NiMo}_6\text{O}_{24}]$ ($\text{NiMo}_6\text{O}_{24}$), $(\text{NH}_4)_3[\text{H}_6\text{CrMo}_6\text{O}_{24}]$ ($\text{CrMo}_6\text{O}_{24}$), $\text{Na}_3[\text{H}_6\text{AlMo}_6\text{O}_{24}]$ ($\text{AlMo}_6\text{O}_{24}$) modified Cu nano materials on TiO_2 nanotube array (TNA) for enhancing HER performance in acidic aqueous solution; the obtained Cu based materials $\text{NiMo}_6\text{O}_{24}@\text{Cu}/\text{TNA}$ possessed dendrites morphology specifically under the current applied condition and showed best activity and long term stability. High specific surface area, surface modification with POMs via Oxygen-Cu bond were obtained via electrochemical co-deposition offering simple pathway to investigate the enhancement due to individual catalyst components. Emphasizing the effect of the electron-proton couple reaction by Anderson type POMs in HER activity based on Cu nano materials. The proposed strategy to fabricate $\text{NiMo}_6\text{O}_{24}@\text{Cu}/\text{TNA}$ and the electrolyzers that show improvement of HER activity and remarkable stability highlighting the effect of POMs modification; which would inspire more effective, low-cost strategies for energy conversion and open the pathway for large scale production.

2. Experimental section

2.1. Materials

$(\text{NH}_4)_4[\text{H}_6\text{NiMo}_6\text{O}_{24}]$ ($\text{NiMo}_6\text{O}_{24}$), $(\text{NH}_4)_3[\text{H}_6\text{CrMo}_6\text{O}_{24}]$ ($\text{CrMo}_6\text{O}_{24}$), $\text{Na}_3[\text{H}_6\text{AlMo}_6\text{O}_{24}]$ ($\text{AlMo}_6\text{O}_{24}$) were synthesized in our lab according to previously published literature [16]. Ammonium molybdate tetrahydrate ($(\text{NH}_4)_6[\text{Mo}_7\text{O}_{24}] \cdot 4\text{H}_2\text{O}$), sodium molybdate dehydrate ($\text{Na}_2\text{MoO}_4 \cdot 2\text{H}_2\text{O}$), nitric acid (HNO_3), nickel nitrate hexahydrate ($(\text{Ni}(\text{NO}_3)_2 \cdot 6\text{H}_2\text{O}$), chromium(III) nitrate nonahydrate ($\text{Cr}(\text{NO}_3)_3 \cdot 9\text{H}_2\text{O}$), aluminum nitrate nonahydrate ($\text{Al}(\text{NO}_3)_3 \cdot 9\text{H}_2\text{O}$) were purchased from Aladdin. Cu foam (20 cm × 20 cm), titanium foils (0.1 cm × 20 cm × 20 cm) were purchased from Oudifu co., Ltd. $\text{Na}_2\text{HPO}_4 \cdot 2\text{H}_2\text{O}$, $\text{Na}_2\text{HPO}_4 \cdot 3\text{H}_2\text{O}$, copper sulfate pentahydrate ($\text{CuSO}_4 \cdot 5\text{H}_2\text{O}$), sulfuric acid (H_2SO_4), ammonium fluoride (NH_4F), ethylene glycol ($(\text{CH}_2\text{OH})_2$), potassium chloride (KCl), were purchased from Sinopharm Chemical Reagent Co., Ltd. Nitrogen was purchased from HUAYUAN chemical co., Ltd. The ultrapure water used in all experiments with a resistivity of 18.2 megaohms was prepared using an ultrapure water system.

2.2. Preparation of TiO_2 nanotubes array (TNA)

High ordered TiO_2 nanotubes array (TNA) was prepared according to the literature [23]. Titanium foils (50 mm × 10 mm × 0.1 mm, 99.99%, Oudifu) were polished by abrasive paper and ultrasonically washed by acetone, ethanol, and ultrapure water for 30 min, respectively. Afterward, the titanium foils were immersed in a mixed solution of HF: HNO_3 : H_2O with volume ratio of 1:4:5 for 30 s, washed by ultrapure water, and dried in a N_2 stream. Anodization of Ti foil was

conducted in an organic electrolyte of ethylene glycol containing 0.5% (w/v) NH_4F and 2% (v/v) H_2O , where the titanium foil was used as a working electrode with a platinum mesh as a counter electrode. The anodization of titanium foil was first carried out at 30 V for 3 h, after which the obtained samples were washed by ultrapure water, dried in a N_2 stream, and subsequently sonicated for 5 min to remove the surface layer; the second anodization was carried out under the same experimental conditions for 3 h. Finally, TNA samples were gently sonicated and annealed at 450 °C in air for 3 h to transform the amorphous phase of TiO_2 to the anatase phase. The obtained tubular graphic structure could offer a large number of sites for next functionalization over external and internal surface.

2.3. Sole Cu deposition on TiO_2 nanotubes array

Electrolytes containing 0.1 M of CuSO_4 were prepared using reagent grade, chlorides free CuSO_4 solution was adjusted to pH = 1 by adding diluted sulfuric acid with ultrapure water [24].

Electrochemical setup was a standard three-electrode cell with the prepared TNA as working electrode, glassy carbon as counter electrode, and saturated calomel electrode (SCE) as reference electrode. Electrochemical experiments were controlled with potentiostat-galvanostat (CH Instruments model 660E). All experiments were performed under constant temperature conditions ($T = 25$ °C). Cyclic voltammetry was used to perform the Cu deposition, the potential ranged from 0.6 V to -0.8 V with scan rate 50 mV s⁻¹ for successive required cycles, TNA with 1 cm² immersed below the working solution. All the potentials in this part were based on SCE reference electrodes.

2.4. Cu deposition with POM on TiO_2 nanotube array

Electrolytes containing 1 mM of $\text{NiMo}_6\text{O}_{24}$, 0.1 M of CuSO_4 were prepared, chlorides free CuSO_4 Solution was adjusted to pH = 1 by adding diluted reagent grade sulfuric acid with ultrapure water. The Cu deposition procedure was the same as the sole Cu deposition. Cyclic voltammetry was used to perform the Cu deposition, the potential ranged from 0.6 V to -0.8 V with scan rate 50 mV s⁻¹ for successive required cycles, TNA with 1 cm² immersed below the working solution (25 °C). All the potentials in this part were based on SCE reference electrodes. The depositions with $\text{AlMo}_6\text{O}_{24}$, $\text{CrMo}_6\text{O}_{24}$ were carried out in similar manner.

2.5. Characterizations

The electrochemical properties of as prepared Anderson type POMs were investigated via cyclic voltammetry by CHI 660e electrochemical workstation with glassy carbon working electrode, SCE reference electrodes and Pt mesh counter electrodes. The phase purity of obtained composites (Cu/TNA , $\text{NiMo}_6\text{O}_{24}@\text{Cu}/\text{TNA}$) characterized by Powder X-ray diffraction (XRD) (D/max 2550 V L/PC) with Cu K_α (1.5418 Å) radiation from 20° to 80° at a scanning rate of 4°/min. The X-ray tube voltage and current were set at 35 kV and 200 mA, respectively. The required samples were scraped off titanium foil by scalpel gently for characterization. Diffraction peak identification was performed based on the JCPDS database of reference compounds. The relative XRD patterns of TiO_2 (Anatase) was identified by comparisons with their respective standard PDF#21-1272. The XRD pattern of Cu was identified by comparisons with their respective standard PDF#04-0836.

The particles sizes and external morphologies of obtained $\text{NiMo}_6\text{O}_{24}@\text{Cu}/\text{TNA}$ $\text{SiW}_{12}\text{O}_{40}@\text{Cu}/\text{TNA}$ were characterized by HORIBA SU 8010 scanning electron microscope along with element mapping distributions investigated by EDX at high voltage 15 KV and working distance 15 mm. The detailed morphology, crystal lattice fringe of the POMs@Cu/TNA catalysts were examined by a HITACHI H-7700 TEM with an accelerating voltage of 100 kV, and a JEOL 2100 F HRTEM operating at 200 kV.

The oxidation state of the prepared composites was obtained by X-ray photoelectron spectroscopy (ULVAC-PHI Quantera SXM) under GB/T 19500-2004 X-ray photoelectron spectroscopy method, Al (200 μm), pass energy: 55 eV, step width: 0.1 eV, incident angle: 45°, Analysis room vacuum degree: 1.0×10^{-7} Torr. Sputtering conditions: gun Ar⁺, SiO₂/Si. The spectra were obtained with photon energy of 1486.7 eV (Al anode). All the binding energies were referenced to the C1s peak at 284.8 eV of the surface adventitious carbon.

Raman scattering spectroscopy was performed on a Horiba LabRam HR-UV 800/Jobin-Yvon equipment, equipped with a He-Ne laser ($\lambda = 633$ nm) with 10 mW of intensity, a CCD detector and an Olympus BX41 microscope with a 100 \times objective.

The real percentage of Cu was measured with inductively coupled plasma atomic emission spectroscopy (ICP-AES) using an ICP AES (iCAP Q, Thermo, Waltham, USA). The detection limit of ICP spectrometer is 20 ppb Cu.

2.6. Electrochemical measurements

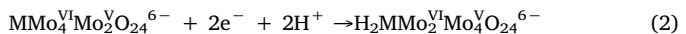
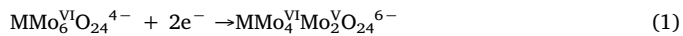
All electrochemical properties were investigated on a CHI 660e electrochemical workstation in a classic three-electrode configuration cell using TNA, glassy carbon electrode, Pt mesh, as-prepared NiMo₆O₂₄@Cu/TNA, as the working electrode, respectively; glassy carbon slide ($3 \times 1 \text{ cm}^2$) as the counter electrode, and SCE as the reference electrode in pH = 6.8 phosphate buffer or 0.5 M H₂SO₄ aqueous electrolyte, whereas the geometric active area was precisely controlled at $1 \times 1 \text{ cm}^2$. HER polarization curves were collected at a scan rate of 1 mV s⁻¹ via LSV. Before the measurement, the working solution was purged with N₂ for 40 min to remove dissolved oxygen with flow rate of 150 mL/min. The Nyquist plots were measured with frequencies ranging from 100 kHz to 0.1 Hz, and the amplitude of the applied voltage was 1 mV. The impedance data were fitted to a simplified Randles circuit to extract the charge-transfer resistances. In all measurements, we used SCE as the reference. It was calibrated with respect to RHE. In 0.5 M H₂SO₄, E (RHE) = E (SCE) + 0.2412 + pH × 0.0592. Overpotential (V) = E (RHE) - E_0 (H⁺ / H₂). E_0 (H⁺ / H₂) is the reduction potential for H⁺ / H₂ (0 V versus RHE). All the electrolysis was conducted at room temperature, and 85% IR correction was applied in all measurements.

3. Results and discussion

3.1. Electrochemical properties and textural investigation

As is well known, Anderson type heteropolyoxomolybdates are built of six edge-sharing MoO₆ octahedral surrounding a central templating edge-sharing octahedrally coordinated heteroatom; Al^{III}, Cr^{III}, and Ni^{II} as central heterometals which have been mostly studied [25]. The related IR spectra of as-prepared (NH₄)₄[H₆NiMo₆O₂₄], (NH₄)₃[H₆CrMo₆O₂₄], Na₃[H₆AlMo₆O₂₄] are shown in Figure S1 (ESI). The observed peaks are all well matched characteristic peaks of the typical Anderson type POMs which ensure the successful synthesis confirming the purity of the as-prepared Anderson type POM compounds [26,27].

The electrochemical behaviours of the three Anderson type POMs were studied by cyclic voltammetry (CV) and compared to each other. Cyclic voltammograms are represented in Fig. 1 A, the separation between the anodic and the cathodic peaks of the redox processes $E_{p1/2}$ are gathered in Table 1 (ESI). Plots of the peak current i_{pc} and i_{pa} versus the square root of the scan rate $v^{1/2}$ for the reversible processes are also given in Figures S3 (ESI). As known for Anderson type POMs, the observed two well-defined reversible of two-electron transfer redox waves are observed where the reduced reactions are related to following electrochemical process:



As shown in Table 1 (ESI), the $E_{p1/2}$ of the first Mo^{VI/V} redox peak appeared up to -17 mV with AlMo₆O₂₄, which is the most positively early reduced wave among three as-prepared POMs (-37 mV for NiMo₆O₂₄, -39 mV for CrMo₆O₂₄). This presented remarkable two-electron transfer ability because the first wave is only electrons participated. While the second redox peak of Mo^{VI/V} is depended on electron-proton coupled reaction; the onset potential of expected HER by multiple components integrated complex catalysts can be directly managed with the $E_{p1/2}$ of the electro-proton coupled reaction because it would improve the underpotential adsorption region to most positive direction on working potential window for Pt free catalysts; about the three as-prepared POMs, the $E_{p1/2}$ of the second redox peak is -338 mV for CrMo₆O₂₄, -345 mV for NiMo₆O₂₄, -353 mV for AlMo₆O₂₄. However, considering electron transfer ability and proton adsorption both, NiMo₆O₂₄ shown the moderate $E_{p1/2}$ about the two observed redox peaks of Mo^{VI/V}, not with one outstanding and the other inferior; hence, the prediction of related strategy with NiMo₆O₂₄ which would show the best performance upon HER under same condition was made.

As is well known, the electronic structure, binding and surface energy of catalysts are strongly related to their morphologies. For heterogeneous catalysis reaction, specific morphologies are essential for desired performance. The obtained TiO₂ nanotube array (TNA) via twice anodization possessed highly ordered nanotubular morphology with ~100 nm diameter (wall thickness ~25 nm) and rough tube wall surface (Figure S2, ESI) which could offer high specific surface area and attachment sites for the next Cu electrochemical deposition. In addition, the powder X-ray diffraction (XRD) pattern indicated the obtained TNA had high crystalline phase corresponding to single crystal anatase dominated by the thermodynamically stable {101} facets (Fig. 1 B, black curve) which is with good surface stability and conductivity (Anatase PDF#21-1272). [28] The unique properties of the as-prepared TNA endow it a proper catalyst support for current strategy. Afterward, POMs@Cu/TNA were fabricated through cyclic voltammetry co-electrochemical deposition, the CVs in Figure S4 (ESI) shown characteristic redox peaks of POMs and Cu reduction plus well-defined copper nucleation behaviours conforming successful co-deposition with Cu and POMs meanwhile POMs keeping its intrinsic electrochemical properties. Therefore, this electrochemical deposition occurred with POMs and Cu NPs simultaneously deposited on TNA supports; the corresponding morphologies, chemical oxidation station and electronic structures of obtained Cu based nano materials must be modified with these different transition metals centred POMs (M = Al, Cr, Ni). However, the crystalline nature of obtained POMs@Cu/TNA was investigated with XRD showing diffraction peaks mainly located at $2\theta = 43.3$, 50.43, and 74.13, attributable to the {111}, {200} lattice planes of Cu and {311} lattice plane of Cu₂O (PDF#04-0836). At the meantime, the XRD pattern of TNA was also existed and no changes in all samples indicating TNA was suitable catalysts support for electrocatalytic processes since no phase changes during electrochemical deposition. This would guarantee related stability of the as-prepared catalysts.

Morphologies of Cu based catalysts were characterized with scanning electron microscopy (SEM) images. Bulk particles with heavy aggregations on the top of TiO₂ nano tube array were observed on Cu/TNA (Figure S5, ESI), this crystallization behavior was usually taken place in static solution which was in consistent with previously reported [29]. While with POMs addition, different morphologies were achieved, as can be seen from Figure S5 (ESI), smaller nano particles with much aggregations were still existed with AlMo₆O₂₄ and CrMo₆O₂₄. The dendrite-like morphologies were exhibited when the co-deposition was carried out with NiMo₆O₂₄ under same electrochemical co-deposition protocol. The specific morphology was depended on the unique electrochemical properties of its proper redox potential and current

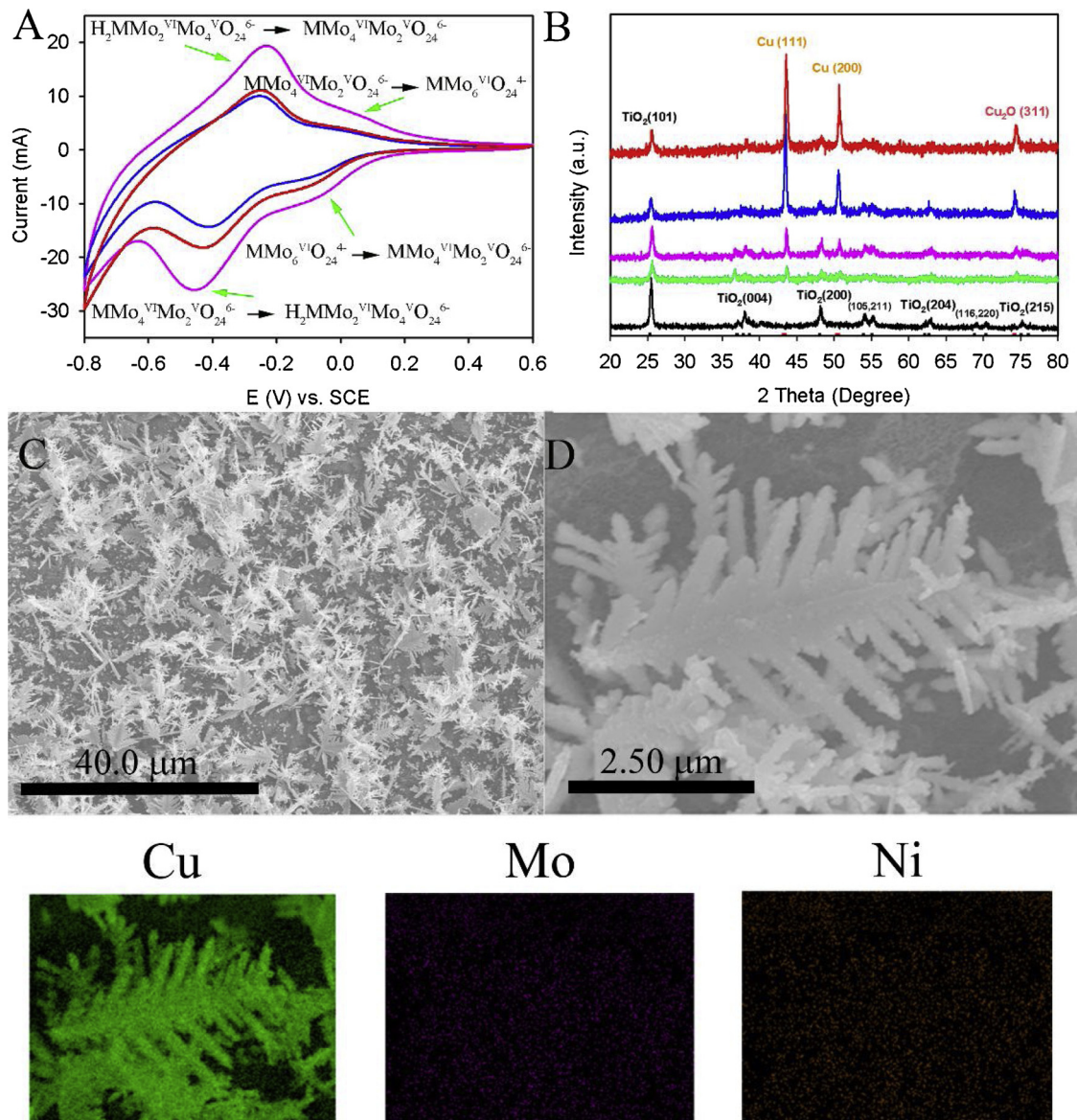


Fig. 1. A) CVs of $\text{NiMo}_6\text{O}_{24}$ (red curve), $\text{AlMo}_6\text{O}_{24}$ (purple curve), $\text{CrMo}_6\text{O}_{24}$ (blue curve) in 0.5 M H_2SO_4 , 0.5 M Na_2SO_4 ; B) XRD of the obtained $\text{NiMo}_6\text{O}_{24}$ @Cu/TNA 5 cycles (red curve), $\text{CrMo}_6\text{O}_{24}$ @Cu/TNA 5 cycles (blue curve), $\text{AlMo}_6\text{O}_{24}$ @Cu/TNA 5 cycles (purple curve), Cu/TNA 5 cycles (GREEN curve) and TNA (Black bar: Anatase PDF#21-1272; red bar: Cu PDF#04-0836); C) Cu dendrites and particles on TNA; D) Cu dendrite branches. The images below are Cu, Mo Ni Elements distribution over (C). (For interpretation of the references to colour in this figure legend, the reader is referred to the web version of this article).

densities under current condition.

The obtained dendrites morphologies are shown in Fig. 1 C and D, integrated fishbone-like particles are composed of an array of columns along different directions, which is attributed to the preferential crystal growth along $\{110\}$ direction. About the morphology formation process, at the beginning of the electrochemical deposition, Cu grows on the surface of TiO_2 nanotubes to form particles layers which will fill the interval space among these nanotubes (Figure S7 A, ESI). When the Cu particles fully cover the top of TNA, sprout of Cu dendrites starts to show up because the loaded Cu particles highly increase the conductivity of TNA substrate leading to an increased deposition current. This accelerates the deposition rate of Cu^{2+} ions being reduced to Cu atoms with a cathodic potential and leads to the precipitation of Cu atoms along the close-packed directions (110 direction) in order to minimize the system energy, thus, form the Cu lattice crystal. Finally, branches of the dendrite were developed on the primary ones to different directions.

Fig. 2 A shows the HRTEM of obtained Cu dendrites revealing

crystallographic growth direction and the clear lattice fringes within interplanar distance of 0.21 nm, corresponding to the $\{111\}$ plane of Cu, which is consistent with the XRD pattern showed single crystal dominated by the $\{111\}$ facets in Fig. 1B. The relative FFT of Cu dendrites in Fig. 2 B provides better understanding confirming the single crystal structures of the catalysts. Indeed, $\text{NiMo}_6\text{O}_{24}$ mass transfer is enhanced around TNA electrode. With the diffusion of the $\text{NiMo}_6\text{O}_{24}$ POMs along Cu deposition, the apexes of Cu particles, which protrude into the region of higher Cu^{2+} concentration, grow faster than the central parts of the facets and thus; branches are formed (Figure S7 B, C, D, ESI) and finally the dendrites with surface covered by $\text{NiMo}_6\text{O}_{24}$; the specific morphology of dendrites would offer sufficient active sites and improved mass transfer for HER. Otherwise, the presence of $\text{NiMo}_6\text{O}_{24}$ could be confirmed by the related energy dispersive X-ray element mapping in Fig. 1 and Figure S6 visually, it also can be seen from the X-ray photoelectron spectroscopy (XPS) (Fig. 3) and corresponding Raman spectrum (Fig. 4).

X-ray photoelectron spectroscopy (XPS) was used to characterize

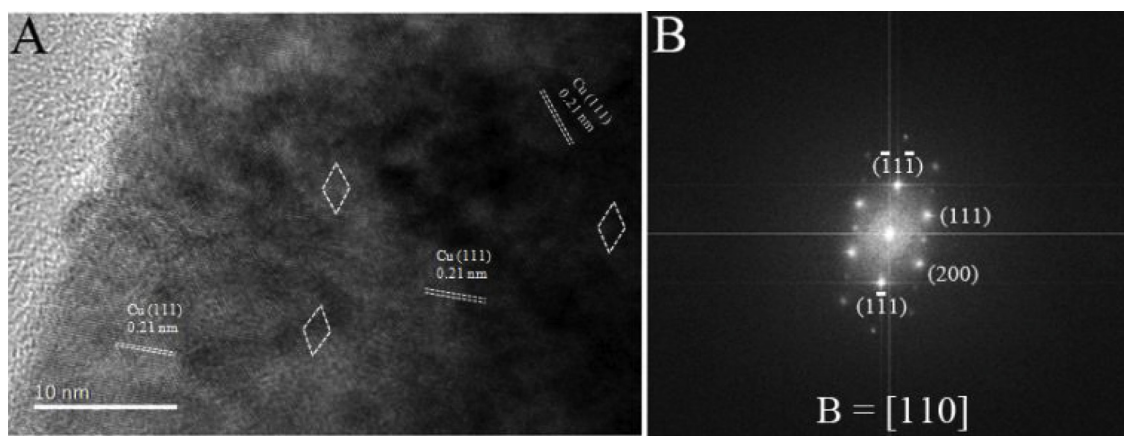


Fig. 2. A) HRTEM of the obtained Cu dendrites; B) Selected area electron diffraction pattern of Cu dendrites.

the atomic valence states and composition of the prepared Cu/TNA and POMs@Cu/TNA because of the relevant catalytic activity is closely correlated to its chemical environment. As shown in Fig. 3A, Cu 2p_{1/2} and Cu 2p_{3/2} located at 951.71 eV, 931.90 eV with weak satellite feature around 945.00 eV confirmed the Cu¹ existence on the surface of Cu/TNA; related Cu LMM auger spectra shown in Fig. 3B, the deconvoluted peak located at 916.50 eV dominated the main Cu LMM region of Cu/TNA which is corresponding to Cu¹, while peak at 918.76 eV represented Cu⁰ which meant the exposed bulk Cu NPs were easily oxidized even with inevitable CuO contamination without additive protectors, the obtained Cu⁰/Cu¹ ratio is only 0.31. After POMs addition, the presence of Cu⁰ in POMs@Cu/TNA can be confirmed by the XPS spectra, the characterized Cu 2p peaks were 932.74 eV, 952.54 eV for AlMo₆O₂₄@Cu/TNA; 932.64 eV, 952.46 eV for CrMo₆O₂₄@Cu/TNA and 932.64 eV, 952.44 eV for NiMo₆O₂₄@Cu/TNA. [30] Thus, Fig. 3A does not show satellite peaks around 945.00 eV which are characteristic of oxidized Cu¹. In other words, if Cu¹ would present a weak satellite feature which would be recorded at these energies, this is not our case

here. Moreover, in Fig. 3B related Cu auger region, the obvious binding energy located at 918.62 eV standing for the existence of Cu⁰ compared to the one of Cu/TNA, the ratio of Cu⁰/Cu¹ highly increased to 2.28. Therefore, the XPS spectra clearly confirmed the obtained Cu NPs were composed of mainly Cu⁰ chemical state but with few Cu₂O contaminated over the surface. The still existence of Cu¹ we predicted it was because of the association with POMs and Cu NPs which the oxygen bonded to Cu during the electrochemical co-deposition course leading to the valence change of Cu⁰. That meant the adsorption of POMs on the surface of as-prepared Cu NPs is not only depended on electrostatic adsorption, but chemical association must be formed between POMs and Cu NPs. POMs modification can prevent the Cu based nano NPs from oxidation no matter the different morphologies they have. This will be evidenced through Raman investigation about all the obtained Cu based nano materials in this work.

About the intact of POMs on the surface of Cu NPs, we took NiMo₆O₂₄@Cu/TNA as example. As is shown in Fig. 1C, Ni 2p_{1/2} peak at 873.73 eV and the Ni 2p_{3/2} peak at 856.16 eV along with the high

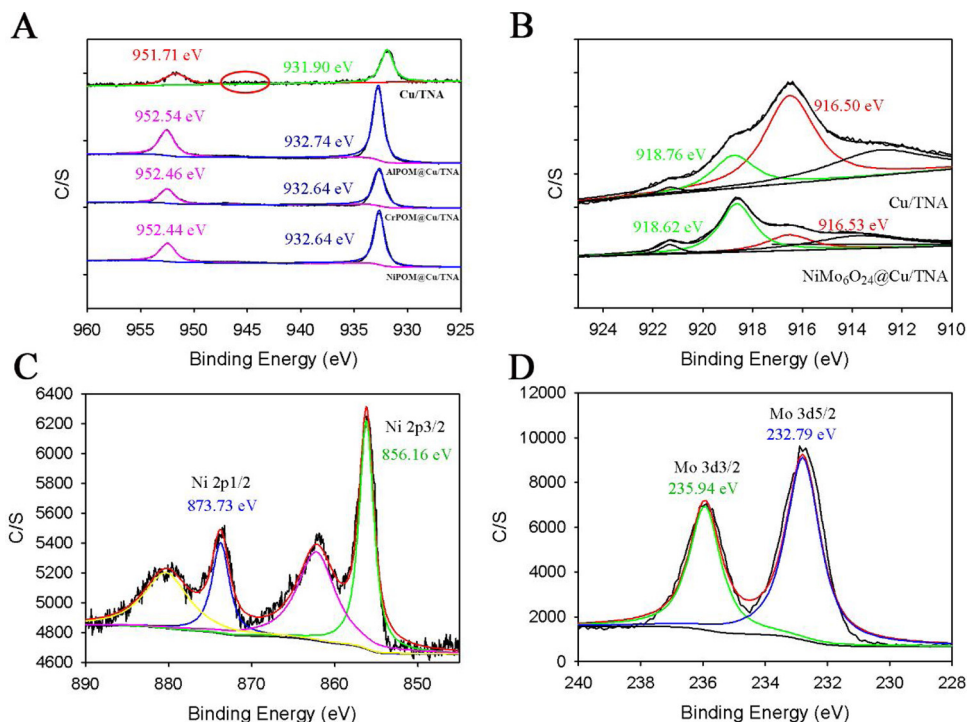


Fig. 3. A) XPS spectra of Cu/TNA, AlMo₆O₂₄@Cu/TNA, CrMo₆O₂₄@Cu/TNA and NiMo₆O₂₄@Cu/TNA; B) Cu LMM region of Cu/TNA and NiMo₆O₂₄@TNA; C) and D) XPS of Ni, Mo in NiMo₆O₂₄@Cu/TNA slide. All electrodeposition is with 5 cycles.

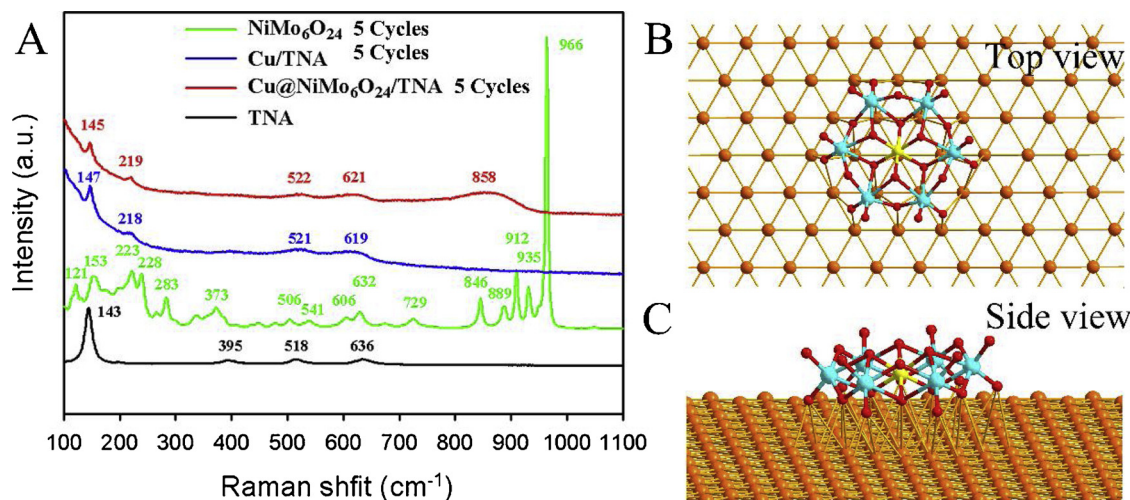


Fig. 4. Raman spectra of A) TNA, NiMo₆O₂₄, Cu/TNA and NiMo₆O₂₄@Cu/TNA; B) and C) Top view, side view of chemical association simulation of Anderson type polyoxometalates on Cu {111} surface schemes. All electrodeposition is done with 5 cycles.

revolution Mo 3d spectrum (Fig. 3 D) which was mainly deconvoluted into two peaks located at 235.94 eV and 232.79 eV according to the highest oxidation state of Mo^{VI} indicated NiMo₆O₂₄ keeping its original oxidative state over Cu dendrites [31,32]. XPS spectrums of Al 2p and Cr 2p also confirmed the intact of related POMs on AlMo₆O₂₄@Cu/TNA and CrMo₆O₂₄@Cu/TNA (Figure S8, ESI). In addition, the O1s spectrum showing peak at 530.33 eV exhibited the characteristic of metal oxides in pure POMs (Figure S9, ESI) [33].

To elucidate the precise structures of obtained POMs@Cu/TNA and to support the chemical association presence between POMs and Cu or TNA, further investigation of Raman spectroscopy was performed and the results are presented in Fig. 4. As depicted in Fig. 4 A (Black curve), TNA shows characteristic Raman active peaks at 143, 395, 518, 636 cm⁻¹, corresponding to the existence of anatase phase, detail curve is in Figure S10 A [34,35]. The bands located at 966, 935, 912, 889, 846, 729, 632, 541, 506, 373, 228, 223 153 cm⁻¹ are ascribed to the Anderson type POMs, here is identified for NiMo₆O₂₄. 966 cm⁻¹ referred to $\nu_s(\text{Mo} = \text{O}_\text{f})$, 541, 506, 373, 228, 223 153 cm⁻¹ referred to $\nu_{as}(\text{Mo-O}_\text{b}-\text{Mo})$ and $\nu_{as}(\text{Mo-O}_\text{c}-\text{Mo})$ [36–39]. As shown in Figure S10 B, similar typical characteristic peaks were observed on CrMo₆O₂₄ (Blue curve) and AlMo₆O₂₄ (Purple curve), respectively. When Cu NPs were deposited on TNA, the Raman spectrum of Cu/TNA was like the one of TNA but with new peak appeared at 218 cm⁻¹; otherwise, the peak located at 143 cm⁻¹ decreased which mean the surface of TNA was covered with Cu NPs changing surface phases because this peak was due to crystal scattering parasite. Furthermore, the obtained NiMo₆O₂₄@Cu/TNA shown similar characteristic peaks like Cu/TNA with a new wide peak at 858 cm⁻¹, this situation was also observed with the control group of POMs: CrMo₆O₂₄@Cu/TNA (red curve), Al-Mo₆O₂₄@Cu/TNA (black curve) in Figure S10 C. As aforementioned, the adsorption of POMs on Cu NPs is due to electrostatic force and chemical association. Herein, the peak at 858 cm⁻¹ of NiMo₆O₂₄@Cu/TNA is predictably referred to the association of characteristic peaks located around 966 cm⁻¹ on to Cu NPs surface, according to the molecular structure of Anderson type POMs and the {111} crystal face dominated Cu dendrites, where the 6 downward terminal Mo = O bonds, 6 bridge Mo-O-Mo bonds would share oxygen atom with surface Cu atom to form Mo-O-Cu bond resulting in related Raman peak shift to lower wavelength. The simulation bonding schemes of the obtained Mo-O-Cu bonds between POMs and Cu {111} surface is shown in Fig. 4B (Top view) and C (Side view). Herein, it is reasonable to believe that strong POM-Cu bonding interaction formed on the Cu based catalysts through the terminal oxygen sites which may distort the molecular structure of the bound POMs and the intrinsic heterogeneity of

this surface bonding to certain degree causing an overlap of the $\nu_s(\text{Mo} = \text{O}_\text{f})$ with $\nu_{as}(\text{W-O}_\text{c}-\text{Cu})$ vibrational peaks. Therefore, we assign the broader band at 858 cm⁻¹ to contributions from both $\nu_s(\text{Mo} = \text{O}_\text{f})$ and $\nu_{as}(\text{W-O}_\text{c}-\text{W})$ vibrations. Plus, the simultaneous observation of several Raman peaks located at 621, 552, 219 cm⁻¹ attributable to $\nu_{as}(\text{Mo-O}_\text{b}-\text{Mo})$ and $\nu_{as}(\text{Mo-O}_\text{c}-\text{Mo})$ of the POMs which might also due to that bridge oxygen association with Cu; 145 cm⁻¹ attributable to crystal scattering from both TNA and Cu based dendrites NPs which illuminate the overall molecular structure of as-prepared POMs@Cu/TNA. Such structure strategy would offer efficient electrons transfer pathway, H atom adsorption sites and related catalyst stability under HER process.

3.2. Improved HER performance and proposed mechanism

The activity of as-prepared POMs@Cu/TNA toward HER was investigated to evaluate the effect of POMs modification. As shown in Fig. 5A, the as-prepared NiMo₆O₂₄@Cu/TNA was applied in electrochemical hydrogen evolution reaction as electrocatalyst under acidic aqueous solution. The HER activity turned out to increase with successively increased Cu deposition cycles that the overpotential shift to more positive direction in fresh 0.5 M H₂SO₄ solution. Moreover, the performance at 10 mA cm⁻² reached platform as the deposition cycle number n = 5 (Fig. 5B) because of more Cu deposition load leading to the decrease of specific surface area and the relevant H⁺ mass transfer issue. Afterward, the HER performance was carried out with the control groups, as shown in Fig. 5C, the overpotential at 10 mA cm⁻² was positively shifted by 66 mV, 130 mV compared to Cu/TNA and Cu foam, respectively, but 75 mV negatively shifted compared to pure Pt wire. Compared to the control group of CrMo₆O₂₄@Cu/TNA and Al-Mo₆O₂₄@Cu/TNA, the improvement is apparent with 20 mV. Ni-Mo₆O₂₄@Cu/TNA is no doubt the best electrocatalysts under current Pt free HER strategy; although, it is not comparable to Pt catalyst, the obvious improvement cannot be disregarded [38–44]. Otherwise, the catalysts with POMs modification they all exhibited superior performance than the bare Cu foam and as-prepared Cu/TNA which obviously emphasize the effect of POMs including the morphology control, electron transfer ability and H adsorption. (Table S3)

In order to understand the unique electrochemical properties of the NiMo₆O₂₄@Cu/TNA, further analyses of the electrochemically active surface areas (ECSAs) of NiMo₆O₂₄@Cu/TNA were investigated using double layer capacitance of potential windows where double-layer charging and discharging is relevant (Figure S11, ESI). The correlation analysis showed that NiMo₆O₂₄@Cu/TNA had the highest roughness

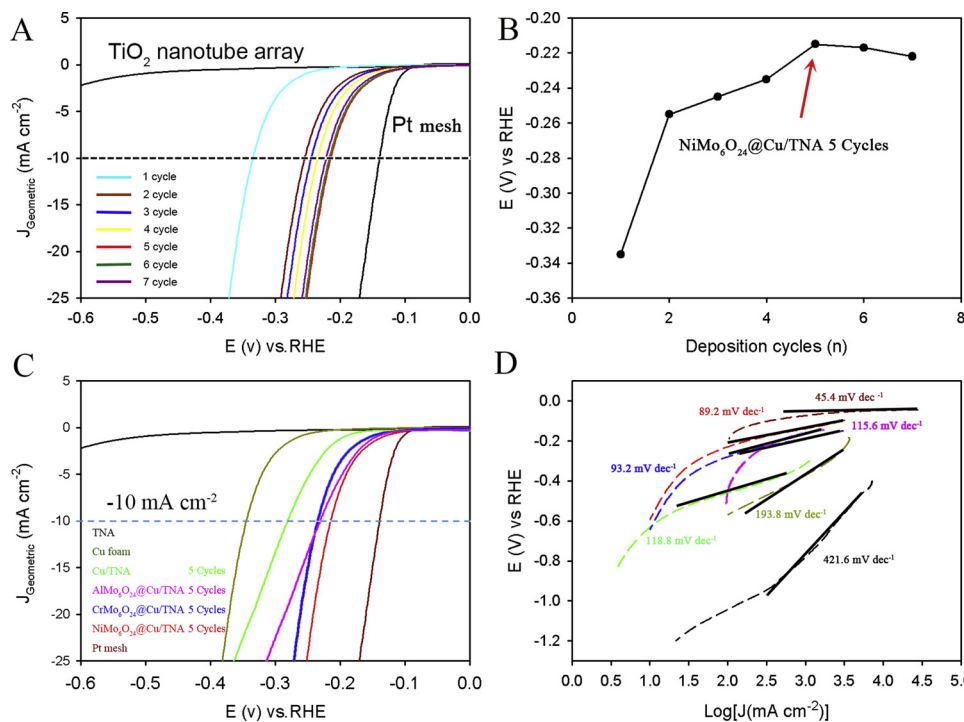


Fig. 5. A) LSV comparison of the NiMo₆O₂₄@Cu/TNA with successive deposition cycles and Pt mesh in 0.5 M H₂SO₄, Scan rate: 1 mV s⁻¹; B) Correlation curve of the potential at 10 mA cm⁻² as function of deposition cycles; C) LSV comparison with TNA slide (black curve), Cu foam (dark green curve), Cu/TNA (green curve), AlMo₆O₂₄@Cu/TNA (blue curve), CrMo₆O₂₄@Cu/TNA (purple curve), NiMo₆O₂₄@Cu/TNA (red curve) and Pt mesh (dark red curve) in 0.5 M H₂SO₄, Scan rate: 1 mV s⁻¹. D) Tafel plots of relevant TNA slide (black curve), Cu foam (dark green curve), Cu/TNA (green curve), AlMo₆O₂₄@Cu/TNA (blue curve), CrMo₆O₂₄@Cu/TNA (purple curve), NiMo₆O₂₄@Cu/TNA (red curve) and Pt mesh (dark red curve) (For interpretation of the references to colour in this figure legend, the reader is referred to the web version of this article).

factor, about 4 times rougher than Cu/TNA and 300 times rougher than the pristine Cu mesh; such surface roughness could offer adequate active sites for the relative HER (Table S2, ESI). Faster electron transfers from NiMo₆O₂₄@Cu/TNA than Cu/TNA was further confirmed with the Nyquist plot of the impedance spectrum, the diameter of Nyquist plot semicircle showed smallest value indicating that the Cu dendrites with NiMo₆O₂₄ had the best electronic conductivity between NiMo₆O₂₄@Cu/TNA and electrolyte which is also the evidence for improved H atom adsorption. (Figure S12, ESI) Otherwise, the corresponding Cu loadings with and without POMs were investigated by ICP-AES, as shown in supporting information Table S4, NiMo₆O₂₄@Cu/TNA had 3 times of Cu loading compared to Cu/TNA which indicated NiMo₆O₂₄ was favorable for Cu deposition meanwhile improving the conductivity by advanced self-reduction.

Furthermore, the kinetic of HER of the applied Cu-based catalysts were evaluated with Tafel plots (Fig. 5D). NiMo₆O₂₄@Cu/TNA catalyst showed the smallest Tafel slope of 89.2 mV dec⁻¹ among Cu based catalysts in this work, although it is higher than the Tafel slope of 20% Pt/C in the literature [45]. Tafel equation can be used to describe the current-potential relationship at a significant over-potential (η):

$$\eta = b \log(j/j_0)$$

where j is the current density, j_0 is the exchange current density and b is the Tafel slope. As it is well known, a slow discharge reaction in HER which is the first step so called Volmer reaction, no matter how effective it can be the formation of H₂ via Volmer-Heyrovsky pathway or Volmer-Tafel pathway, the Tafel slope should be 4.6 RT/F, that is, 116 mV dec⁻¹ at 25 °C.¹² In our case, Cu/TNA showed similar value of Tafel slope which indicated that Cu has poor ability to absorb H atom even though it can release H₂ easily, polycrystalline Cu foam shown even higher Tafel slope which is 193.8 mV dec⁻¹. Based on the difference of Tafel slopes between NiMo₆O₂₄@Cu/TNA and Cu/TNA, under same current density, the related exchange current density was twice folded of NiMo₆O₂₄@Cu/TNA to Cu/TNA. Such remarkable enhancement on overpotential and exchange current density emphasized the effect of NiMo₆O₂₄ which located on the surface of Cu based catalyst accelerating the electron transfer and H⁺ adsorption.

3.3. Corrosion resistance and related stability

Operating under acidic aqueous condition, corrosion resistance is one of the most significant parameters affecting the performance of HER including the activity and stability, especially when the related electrocatalysts have hydrophilic surfaces in consideration of water management. Notably in current work, POMs coating can initially function as an efficient electronic transport layer for HER and serve the initial activation processes as the out most layer. Potentiodynamic polarization was carried out with NiMo₆O₂₄@Cu/TNA and other control groups under pH = 1 and pH = 6.8 aqueous condition, respectively. Here, the potentiodynamic polarization curves in pH = 1 H₂SO₄ condition is plotted in Fig. 5A; corrosion current at -0.6 V vs. SCE is -1.85 A cm⁻², which is much lower than the bare Cu/TNA but higher than Pt mesh samples; similar observation is obtained when HER was operated under pH = 6.8 phosphate buffer. Relatedly, corrosion current is introduced to further qualitatively investigate the anticorrosion ability of coatings according to the calculated protective efficiency (P_i): [46]

$$P_i = \left(1 - \frac{i_{corr}}{i_{corr}^0} \right) \times 100\%$$

where P_i is the protective efficiency of POMs coatings and i_{corr} and i_{corr}^0 refer to the corrosion current of the NiMo₆O₂₄@Cu/TNA and bare Cu/TNA substrate, respectively. Therefore, POMs modification decreased the i_{corr} increasing the protective efficiency compared to bare Cu/TNA which made NiMo₆O₂₄@Cu/TNA stronger corrosion resistance under applied condition. Moreover, the open-circuit potentials are all improved to positive direction after POMs modification which mean POMs coatings decreased the onset-potential due to its significant electron transfer efficiency [47].

Furthermore, the stability of NiMo₆O₂₄@Cu/TNA during HER was evaluated by repeating LSV runs in 0.5 M H₂SO₄ between 0.8 V and -0.6 V vs. SHE. After 500 runs, it exhibited negligible measurable loss of HER activity, overpotential at -10 mA cm⁻² negatively shifted by only 7 mV (Fig. 5 C). The as-prepared NiMo₆O₂₄@Cu/TNA system showed no obvious current decrease under -0.2 V vs. RHE for 3 h, indicating remarkable durability upon HER (Fig. 5 D). In addition, with NiMo₆O₂₄ on the surface as stabilizer, the morphology of

$\text{NiMo}_6\text{O}_{24}$ @Cu/TNA after HER catalysis exhibited no obvious changes which guaranteed the good stability. (Figure S13 ESI)

4. Conclusion

In conclusion, improved HER has been achieved with $\text{NiMo}_6\text{O}_{24}$ @Cu/TNA as an electrocatalyst which is fabricated by co-electrodeposition with Anderson-type POM $\text{NiMo}_6\text{O}_{24}$. Compared to the control groups, the $\text{NiMo}_6\text{O}_{24}$ polyoxoanions participate in the concentric diffusion field of Cu nucleation leading the dendrites morphology formation to provide high specific surface area with exposing more active sites and contribute to modify the local chemical environment of Cu dendrites in electrochemistry. In acidic aqueous solution, POMs act as Brønsted acid to improve the H^+ mass transfer and further help the H atom absorption which remedies the weakness of insufficient H atom absorption ability of Cu based catalysts. When undergoing negative potential scan, $\text{NiMo}_6\text{O}_{24}$ first gets reduced itself and could transfer electrons to accelerate the next absorbed H atom formation and successive H_2 release lowering over-potential upon HER. With the help of $\text{NiMo}_6\text{O}_{24}$, the ability of electrocatalytic HER using Cu based catalysts is highly enhanced by decreasing over-potential with 130 mV compared to Cu foam, Tafel slope decrease from 193.8 mV dec^{-1} to 89.2 mV dec^{-1} . In this work, the proposed $\text{NiMo}_6\text{O}_{24}$ @Cu/TNA strategy possessed improved activity and long term stability upon HER, and meanwhile emphasized the effect of the POM modification. Depending on the diversity of POMs, the current feasible and reliable heterogeneous electrocatalysts design with POMs would inspire more effective strategies for energy conversion and open the pathway for large scale production.

Acknowledgement

The work was supported by the National Natural Science Foundation of China (NSFC No. 21801153, 21471087 and 21225103).

Appendix A. Supplementary data

Supplementary material related to this article can be found, in the online version, at doi:<https://doi.org/10.1016/j.apcatb.2019.02.039>.

References

- A.J. Bard, Inner-sphere heterogeneous electrode reactions. Electrocatalysis and photocatalysis: the challenge, *J. Am. Chem. Soc.* 132 (2010) 7559–7567.
- I. Stephens, A.S. Bondarenko, U. Grønbjerg, J. Rossmeisl, I. Chorkendorff, Understanding the electrocatalysis of oxygen reduction on platinum and its alloys, *Energy Environ. Sci.* 5 (2012) 6744–6762.
- B. Rausch, M.D. Symes, G. Chisholm, L. Cronin, Decoupling hydrogen and oxygen evolution during electrolytic water splitting using an electron-coupled-proton buffer, *Nat. Chem.* 5 (2013) 403–409.
- A.S. Bandarenka, M.T.M. Koper, Structural and electronic effects in heterogeneous electrocatalysis: toward a rational design of electrocatalysts, *J. Catal.* 308 (2013) 11–24.
- Z.C. Zhang, B. Xu, X. Wang, Engineering nanointerfaces for nanocatalysis, *Chem. Soc. Rev.* 43 (2014) 7870–7886.
- P. Munnik, P.E. De Jongh, K.P. De Jong, Recent developments in the synthesis of supported catalysts, *Chem. Rev.* 115 (2015) 6687–6718.
- Z. Cai, Y. Wu, Z. Wu, L.C. Yin, Z. Weng, Y.R. Zhong, W.W. Xu, X.M. Sun, H.L. Wang, Unlocking Bi-functional electrocatalytic activity for CO_2 reduction reaction by win-win metal-oxide cooperation, *ACS Energy Lett.* 3 (2018) 2816–2822.
- Y.C. Huang, J. Hu, H.X. Xu, W. Bian, J.X. Ge, D.J. Zang, D.J. Cheng, Y.K. Lv, C. Zhang, J. Gu, Y.G. Wei, Fine tuning electronic structure of catalysts through atomic engineering for enhanced hydrogen evolution, *Adv. Energy Mater.* 8 (2018) 1–11.
- Y. Zheng, Y. Jiao, M. Jaroniec, S.Z. Qiao, Advancing the electrochemistry of the hydrogen- Evolution reaction through combining experiment, *Angew. Chemie. Int. Ed.* 54 (2015) 52–65.
- M. Xia, T. Lei, N. Lv, N. Li, Synthesis and electrocatalytic hydrogen evolution performance of Ni-Mo-Cu alloy coating electrode, *Int. J. Hydrogen Energy* 39 (2014) 797–4802.
- Z. Lin, J. Li, L. Li, L. Yu, W. Li, G. Yang, Manipulating the hydrogen evolution pathway on composition-tunable CuNi nanoalloys, *J. Mater. Chem. A Mater. Energy Sustain.* 5 (2017) 773–781.
- C.G. Morales-Guio, L.A. Stern, X. Hu, Nanostructured hydrotreating catalysts for electrochemical hydrogen evolution, *Chem. Soc. Rev.* 43 (2014) 6555–6569.
- F. Li, L. Zhang, J. Li, X.Q. Lin, X.Z. Li, Y.Y. Fang, J.W. Huang, W.Z. Li, M. Tian, J. Jin, R. Li, Synthesis of $\text{Cu}-\text{MoS}_2$ /rGO hybrid as non-noble metal electrocatalysts for the hydrogen evolution reaction, *J. Power Sources* 292 (2015) 15–22.
- A.A. Dubale, W.N. Su, A.G. Tamirat, C.J. Pan, B.A. Aragaw, H.M. Chen, C.H. Chen, B.J. Hwang, The synergetic effect of graphene on CuO nanowire arrays as a highly efficient hydrogen evolution photocathode in water splitting, *J. Mater. Chem. A* 2 (2014) 18383–18397.
- X.J. Lv, S.X. Zhou, C. Zhang, H.X. Chang, Y. Chen, W.F. Fu, Synergetic effect of Cu and graphene as cocatalyst on TiO_2 for enhanced photocatalytic hydrogen evolution from solar water splitting, *J. Mater. Chem.* 22 (2012) 18542–18549.
- Y. Huang, J. Ge, J. Hu, J. Zhang, J. Hao, Y.G. Wei, Nitrogen-doped porous molybdenum carbide and phosphide hybrids on a carbon matrix as highly effective electrocatalysts for the hydrogen evolution reaction, *Adv. Energy Mater.* 8 (1–9) (2018) 1701601.
- C. Rinfray, S. Renaudineau, G. Izett, A. Proust, A covalent polyoxomolybdate-based hybrid with remarkable electron reservoir properties, *Chem. Commun. (Camb.)* 50 (2014) 8575–8577.
- J. Macht, M.J. Janik, M. Neurock, E. Iglesia, Catalytic consequences of composition in Polyoxometalate clusters with keggin structure, *Angew. Chemie. Int. Ed.* 46 (2007) 7864–7868.
- C. Zhang, Y. Hong, R. Dai, X.P. Lin, L.S. Long, C. Wang, W.B. Lin, Highly active hydrogen evolution electrodes via Co-deposition of platinum and polyoxometalates, *ACS Appl. Mater. Interfaces* 7 (2015) 11648–11653.
- B. Nohra, H.E. Moll, L.R. Albelo, Polyoxometalate-based metal organic frameworks (POMOFs): structural trends, energetics, and high electrocatalytic efficiency for hydrogen evolution reaction, *J. Am. Chem. Soc.* 133 (2011) 13363–13374.
- C.L. Hill, W. Guo, H. Lv, H.J. Lv, Z.Y. Chen, K. Sullivan, S. Lauinger, Y.N. Chi, J.M. Sumliner, T.Q. Lian, Self-assembly of polyoxometalates, Pt nanoparticles and metal-organic frameworks into a hybrid material for synergistic hydrogen evolution, *J. Mater. Chem. A Mater. Energy Sustain.* 4 (2016) 5952–5957.
- I. Ahmed, X. Wang, N. Boualili, N. Boualili, H.L. Xu, R. Farha, M. Goldmann, L. Ruhlmann, Photocatalytic synthesis of silver dendrites using electrostatic hybrid films of porphyrin-polyoxometalate, *Appl. Catal. A Gen.* 447–448 (2012) 89–99.
- F. Xiao, Layer-by-layer self-assembly construction of highly ordered metal- TiO_2 nanotube arrays heterostructures (M/TNTs, m = Au, Ag, Pt) with tunable catalytic activities, *J. Phys. Chem. C* 116 (2012) 16487–16498.
- D. Grujicic, B. Petic, Electrodeposition of copper: the nucleation mechanisms, *Electrochim. Acta* 47 (2002) 2901–2912.
- A. Boulmier, A. Vacher, D.J. Zang, L. Ruhlmann, D. Lorcy, A. Dolbecq, Anderson-type polyoxometalates functionalized by tetrathiafulvalene groups: synthesis, electrochemical studies, and NLO properties, *Inorg. Chem.* 57 (2018) 3742–3752.
- Y. Xia, Y.G. Wei, Y. Wang, H.Y. Guo, A kinetically controlled trans bifunctionalized organoimido derivative of the lindqvist-type hexamolybdate: synthesis, spectroscopic characterization, and crystal structure of $(\text{n-Bu}_4\text{N})_2[\text{trans}-\text{Mo}_6\text{O}_{17}(\text{NAr})_2]$ (Ar = 2, 6-dimethylphenyl), *Inorg. Chem.* 44 (2005) 9823–9828.
- J. Hao, Y. Xia, L.S. Wang, L. Ruhlmann, Y.L. Zhu, Q. Li, P.C. Yin, Y.G. Wei, H.Y. Guo, Unprecedented replacement of bridging oxygen atoms in Polyoxometalates with organic imido ligands, *Angew. Chem. Int. Ed.* 47 (2008) 2626–2630.
- H.G. Yang, C.H. Sun, S.Z. Qiao, J. Zou, G. Liu, S.C. Smith, Anatase TiO_2 single crystals with a large percentage of reactive facets, *Nature* 453 (2008) 630–641.
- J.B. Xue, W. Liang, X.G. Liu, Q.O. Shen, B.S. Xu, Crystallization behavior and formation mechanism of dendrite Cu_2O , *CrystEngComm.* 14 (2012) 8017–8022.
- X. Liu, D. Gregurec, J. Irigoyen, A. Martinez, S. Moya, R. Ciganda, P. Hermange, J. Ruiz, D. Astruc, Precise localization of metal nanoparticles in dendrimer nanosnakes or inner periphery and consequences in catalysis, *Nat. Commun.* 7 (2016) 1–8.
- H.F. Shi, G. Yan, Y. Zhang, H.Q. Tan, W.Z. Zhou, Y.Y. Ma, Y.G. Li, W.L. Chen, E.B. Wang, Ag/Ag x H_3x $\text{PMo}_{12}\text{O}_{40}$ nanowires with enhanced visible-light-Driven photocatalytic performance, *ACS Appl. Mater. Interfaces* 9 (2017) 422–430.
- S. Shao, J. Liu, J. Bergqvist, S. Shi, C. Veit, U. Würfel, In situ formation of MoO_3 in PEDOT: PSS matrix: a facile way to produce a smooth and less hygroscopic hole transport layer for highly stable polymer bulk heterojunction solar cells, *Adv. Energy Mater.* 3 (2013) 349–355.
- Y. Yan, B. Li, W. Li, H. Li, L. Wu, Controllable vesicular structure and reversal of a surfactant-encapsulated polyoxometalate complex, *Soft Matter* 5 (2009) 4047–4053.
- T. Zheng, E. Feng, Z. Wang, X. Gong, Y. Tian, Mechanism of surface-enhanced raman scattering based on 3D Graphene- TiO_2 nanocomposites and application to real-time monitoring of telomerase activity in differentiation of stem cells, *ACS Appl. Mater. Interfaces* 9 (2017) 36596–36605.
- X. Wang, J. Li, X. Gao, Y. Shen, A. Xie, Ordered CdSe-sensitized TiO_2 inverse opal film as multifunctional surface-enhanced Raman scattering substrate, *Appl. Surf. Sci.* 463 (2019) 357–362.
- F.B. Daho, G. Neveux, M. Mouhamadou, P. Vaudon, C. Decroze, D. Carsenat, An operational modified-LINC demonstrator for wireless communication, *Proc. 5th Eur. Conf. Antennas. Propag.* 130 (2011) 480–482.
- S.S. Zhang, N. Zhang, Y. Zhao, T. Cheng, X.B. Li, R. Feng, H. Xu, Z.R. Liu, J. Zhang, L.M. Tong, Spotting the differences in two-dimensional materials-the Raman scattering perspective, *Chem. Soc. Rev.* 47 (2018) 3217–3240.
- G.C. Lica, K.P. Browne, Y.Y. Tong, Interactions between Keggin-type lacunary Polyoxometalates and ag nanoparticles: a surface-enhanced raman scattering spectroscopic investigation, *J. Clust. Sci.* 17 (2006) 349–359.
- H. An, D. Xiao, E. Wang, Y. Li, X. Wang, L. Xu, Open-framework polar compounds:

synthesis and characterization of rare-earth Polyoxometalates $(\text{C}_6\text{NO}_2\text{H}_5)_2[\text{Ln}(\text{H}_2\text{O})_5(\text{CrMo}_6\text{H}_6\text{O}_{24})0.5\text{H}_2\text{O}$ (Ln = Ce and La), *Eur. J. Inorg. Chem.* 5 (2005) 854–859.

[40] J. Jia, W. Zhou, Z.Q. Wei, T.L. Xiong, G.X. Li, L.L. Zhao, X.F. Zhang, H. Liu, J. Zhou, S.W. Chen, Molybdenum carbide on hierarchical porous carbon synthesized from Cu-MoO₂ as efficient electrocatalysts for electrochemical hydrogen generation, *Nano Energy* 41 (2017) 749–757.

[41] P.D. Tran, M. Nguyen, S.S. Pramana, A. Bhattacharjee, S.Y. Chiam, J. Fize, M.J. Field, V. Artero, L.H. Wong, J. Barber, Copper molybdenum sulfide: a new efficient electrocatalyst for hydrogen production from water, *Energy Environ. Sci.* 5 (2012) 8912–8916.

[42] R.S. Vishwanath, S. Kandaiah, Metal ion-containing C₃N₃S₃ coordination polymers chemisorbed to a copper surface as acid stable hydrogen evolution electrocatalysts, *J. Mater. Chem. A Mater. Energy Sustain.* 5 (2017) 2052–2065.

[43] J.X. Feng, J.Q. Wu, Y.X. Tong, G.R. Li, Efficient hydrogen evolution on Cu nanodots-decorated Ni₃S₂ nanotubes by optimizing atomic hydrogen adsorption and desorption, *J. Am. Chem. Soc.* 140 (2018) 610–617.

[44] M. Kuang, Q. Wang, P. Han, G. Zheng, Cu, Co-embedded N-Enriched mesoporous carbon for efficient oxygen reduction and hydrogen evolution reactions, *Adv. Energy Mater.* 7 (2017) 1–8.

[45] M. Zhu, Y. Du, P. Yang, X. Wang, Donor-acceptor porphyrin functionalized Pt nano-assemblies for artificial photosynthesis: a simple and efficient homogeneous photocatalytic hydrogen production system, *Catal. Sci. Technol.* 3 (2013) 2295–2302.

[46] P. Yi, W. Zhang, F. Bi, L. Peng, X. Lai, Enhanced corrosion resistance and interfacial conductivity of TiC_x/a-C nanolayered coatings via synergy of substrate Bias voltage for bipolar plates applications in PEMFCs, *ACS Appl. Mater. Interfaces* 10 (2018) 19087–19096.

[47] C. Bae, T.A. Ho, H. Kim, S. Lee, S. Lim, M. Kim, H. Yoo, J.M. Montero-Moreno, J.H. Park, H. Shin, Bulk layered heterojunction as an efficient electrocatalyst for hydrogen evolution, *Sci. Adv.* 3 (1-9) (2017) 1602215.

Update

Applied Catalysis B: Environmental

Volume 260, Issue , January 2020, Page

DOI: <https://doi.org/10.1016/j.apcatb.2019.117787>



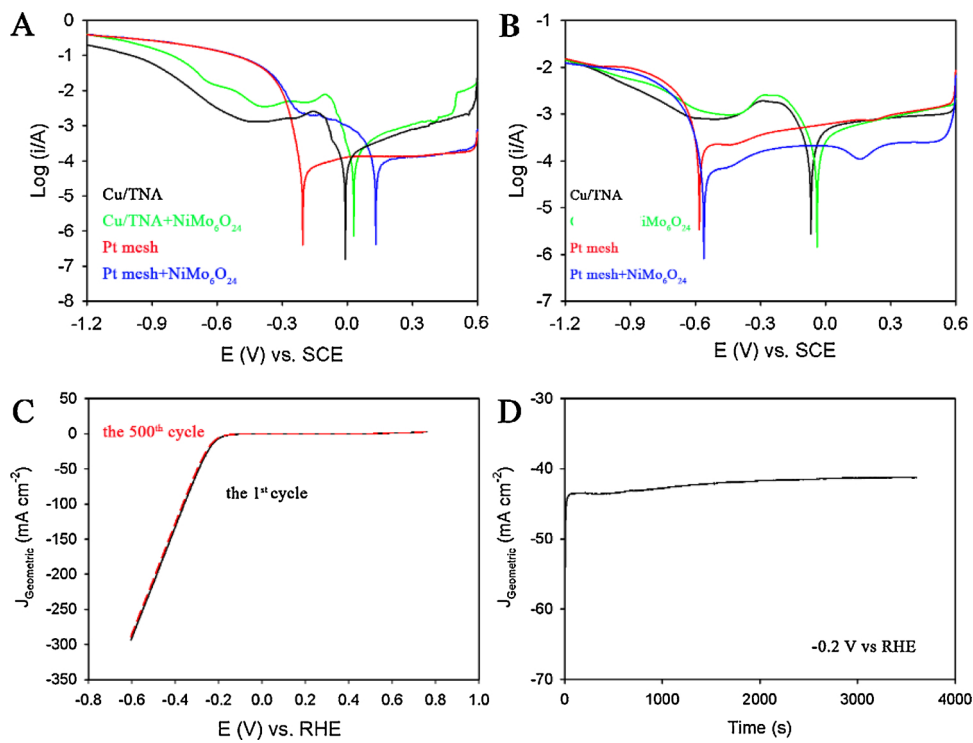
Corrigendum

Corrigendum to “Cu dendrites induced by the Anderson-type polyoxometalate $\text{NiMo}_6\text{O}_{24}$ as a promising electrocatalyst for enhanced hydrogen evolution” [Appl. Catal. B: Environ. 249 (2019) 163–171]

Dejin Zang^a, Yichao Huang^a, Qi Li^a, Yajie Tang^b, Yongge Wei^{a,*}^a Key Lab of Organic Optoelectronics & Molecular Engineering of Ministry of Education, Department of Chemistry, Tsinghua University, Beijing 100084, PR China^b Key Laboratory of Fermentation Engineering (Ministry of Education), Hubei Provincial Cooperative Innovation Center of Industrial Fermentation, Hubei Key Laboratory of Industrial Microbiology, Hubei University of Technology, Wuhan 430068, PR China

The authors regret to leave out one figure in part of **3.3. Corrosion resistance and related stability** of the main text and give the wrong Figure number. There should be Fig. 6 instead of Fig. 5 in this part showing as below:

Fig. 6 A) Potentiodynamic polarization of Cu/TNA, Pt mesh in pH = 1 H_2SO_4 with and without $\text{NiMo}_6\text{O}_{24}$. B) Potentiodynamic polarization of Cu/TNA, Pt mesh in pH = 6.8 phosphate buffer with and without $\text{NiMo}_6\text{O}_{24}$. C) LSV plots in 0.5 M H_2SO_4 with

DOI of original article: <https://doi.org/10.1016/j.apcatb.2019.02.039>

* Corresponding author.

E-mail address: yonggewei@tsinghua.edu.cn (Y. Wei).

scan rate 1 mV/s for the very first cycle (black solid curve) and after 500 cycles (red dash curve); D) i-t curve at -0.2 V verse RHE for 3 h. $\text{NiMo}_6\text{O}_{24}@\text{Cu}/\text{TNA}$ as working electrode, glassy

carbon slide as counter electrode, SCE as reference electrode in all experiments.

The authors would like to apologise for any inconvenience caused.